# PRODEM: Annual summer DEMs (2019-present) of the marginal areas of the Greenland Ice Sheet

Mai Winstrup[1], Heidi Ranndal[1], Signe Hillerup Larsen[2], Sebastian B. Simonsen[1], Kenneth D. Mankoff[2,3,4], Robert S. Fausto[2], Louise Sandberg Sørensen[1]

[1]DTU Space, Technical University of Denmark (DTU), Kgs. Lyngby, 2800, Denmark
[2]Geological Survey of Denmark and Greenland (GEUS), Copenhagen, 2100, Denmark
[3] Autonomic Integra LLC, New York, NY, 10025, USA
[4] NASA Goddard Institute for Space Studies, New York, NY, 10025, USA

*Correspondence to*: Mai Winstrup (maiwin@dtu.dk)

**Abstract.** Surface topography across the marginal zone of the Greenland Ice Sheet is constantly evolving in response to changes in weather, season, climate and ice dynamics. Yet current Digital Elevation Models (DEMs) for the ice sheet are usually based on data from a multi-year period, thus obscuring these changes over time. We here present four 500-meter resolution annual (2019-2022) summer DEMs of the Greenland ice sheet marginal zone (PRODEMs). The PRODEMs cover a 50km wide band from the ice edge, and they capture all outlet glaciers of the Greenland ice sheet. Each PRODEM is based on data fusion of CryoSat-2 radar altimetry and ICESat-2 laser altimetry using a regionally-varying Kriging method. They are validated using leave-one-out cross-validation, showcasing their ability to correctly represent surface elevations within the associated spatially varying prediction uncertainties, which have a median value of 1.4m. We observe a general lowering of surface elevations compared to ArcticDEM, but the spatial pattern of change is highly complex and with annual changes superimposed. The PRODEMs will enable studies of the marginal ice sheet elevation changes in great detail, temporally as well as spatially. With their high spatio-temporal resolution, the PRODEMs will be of value to a wide range of researchers and users studying ice sheet dynamics and monitoring how the ice sheet responds to changing environmental conditions. Incorporating the PRODEM surface elevations in estimates of the solid ice discharge from Greenland outlet glaciers will e.g. improve our assessment of the mass balance of the Greenland ice sheet and its interannual variability. PRODEMs from summers 2019 through 2022 are available at https://doi.org/10.22008/FK2/52WWHG (Winstrup, 2023), and we plan to annually update the product henceforth.

## 1 Introduction

During the past decades, the Greenland Ice Sheet has lost mass at an increasing rate (Otosaka et al., 2023; Shepherd et al., 2020; Simonsen et al., 2021) contributing to globally rising sea levels (Moon et al., 2018; WCRP Global Sea Level Budget Group, 2018). Earth Observation (EO) data are essential to quantify the mass balance of the ice sheet, and one of the geodetic methods applied to EO data to achieve this is the so-called Input-Output method, or mass budget method, which quantifies the imbalance between surface (and basal) mass balance, and the solid ice discharge (King et al., 2020; Mankoff et al., 2021; Mouginot et al., 2019; Van Den Broeke et al., 2009). While the surface mass balance is estimated from Regional Climate Models, the solid ice discharge can be determined from joint observations of ice flow velocity and ice thickness along fluxgates close to the ice sheet grounding line. Basal mass balance is often overlooked, but can be constrained from ice flow models (Karlsson et al., 2021). Two other geodetic methods using EO data are the gravimetry method using data from GRACE and GRACE-FO (Velicogna et al., 2020; Groh et al., 2019), and the volume change method using altimetry (McMillan et al., 2016; Sørensen et al., 2011). The strength of the Input-Output method is that it assesses the individual components of the mass balance, allowing for process studies in high spatial and temporal resolution. With ice flow velocities routinely produced with high accuracy on a bi-weekly basis (Nagler et al., 2015; Solgaard et al., 2021), a major uncertainty associated with the solid ice discharge estimates is related to limited knowledge of the ice thickness along the flux gates near the ice margin. The primary

factor is believed to be errors in bed topography (Mankoff et al., 2019), but changes in ice surface elevations may also play a substantial role.

This paper focuses on the derivation and validation of the PRODEMs. Here, we take advantage of CryoSat-2 and ICESat-2 altimetry data to directly determine the evolving snow-free (summer) ice topography in the ice sheet marginal zone. The annual 500m-resolution DEMs follow the naming convention PRODEMyy, with yy indicating the year, and they form part of the Programme for Monitoring of the Greenland Ice Sheet (PROMICE) project (Ahlstrøm and the PROMICE project team, 2008). Annual assessment of the surface elevation across this rapidly evolving region will eliminate a part of the uncertainty associated with the estimated ice discharge through flux gates used in the Input-Output method. The PRODEMs will thereby allow improved quantification of the annual solid ice discharge of outlet glaciers, leading to more accurate assessments of the mass balance of the Greenland ice sheet and its inter-annual variability.

## 2 Input data

To construct the PRODEMs, we combine summer elevation data from June through September (both months included) from two satellite altimetry missions: ESA's radar mission CryoSat-2 (CS2) and NASA's lidar mission ICESat-2 (IS2). Given the different nature of the sensors of the two satellite systems, their altimetry observations have distinctly different properties, including differences in resolution and topographic sampling, described below. The observed elevations are subsequently transformed to elevation anomalies relative to a reference DEM, for which we use the ArcticDEM v3 mosaic. All elevations are referenced to the WGS84 reference ellipsoid.

### 2.1 CryoSat-2

The SAR Interferometric Radar Altimeter (SIRAL) onboard CS2 has monitored the changes in elevation of the Greenland ice sheet since July 2010 (Parrinello et al., 2018). Here, we primarily use the CS2 SAR interferometry (SARIn) altimetry data from the ice sheet margin. SIRAL has two antennas, and when employed in the advanced SARIn mode, the difference in signal phase received by the two antennas is used to constrain the across-track angle of the first radar returns, whereby the origin of the echo (Point Of Closest Approach; POCA) can be located (Wingham et al., 2006). The observations are relocated from nadir accordingly. This approach enables the instrument to better resolve the relatively rough terrain existing at the ice sheet margin than what is possible from conventional altimetry (Sørensen et al., 2018). In SARIn mode, SIRAL has a footprint of ~400m along-track and 1.65km across-track, which corresponds to a total footprint area of 0.5km$^2$ (ESA, 2019).

We use CryoSat-2 Ice Level 2 Baseline D data (Meloni et al., 2020) for the period until 22 August 2021, after which data from the new Ice Baseline E (ESA, 2021) is available. Ice Baseline E features a range of developments, including improvements to the land ice retracking scheme and resolution of several anomalies in the Ice Baseline D data products. For both data products, we remove data flagged as having issues with accurate elevation retrieval and/or cross-track angle error, and hence geolocation error. Additionally, observations without relocation from nadir or with relocation distances above 15km are considered unrealistic, and these observations are also removed. On average, 23-24% of the original data set is removed, the majority of these having cross-track angle errors. For a small part of the PRODEM area in South West Greenland, CS2 is operated in Low Resolution Mode (LRM) instead of SARIn mode, and for this small area, we include LRM CS2 altimetry data for generating the PRODEMs.

### 2.2 ICESat-2

With the launch of IS2 in September 2018, a new type of satellite altimetry data has become available. The ATLAS instrument
80   onboard IS2 is a single-photon-counting lidar, providing elevation data of extremely high resolution (Markus et al., 2017).
Each track consists of a total of six beams, separated into three pairs, with approximately 3km between pairs, and 90m between
adjacent beams within a pair. Each pair consists of one strong and one weak beam, and given the short distance between them,
the measured elevations along the two beams are strongly correlated. To avoid excessive oversampling of specific areas, we
construct the PRODEMs using data only from the three strong beams.
85

From IS2 we use the Land Ice Height data set ATL06 V5 (Smith et al., 2021). This is a down-sampled product in which
individual photon heights are averaged within 20m segments along each beam (Smith et al., 2019). Data points flagged as bad
data in the data product are removed (3-7% depending on year). Given that the topographic variations to be resolved in the
500m resolution PRODEM are much smoother than 20m, we further down-sample the ATL06 data by computing median
90   values over 250m along-track segments of each beam. Segments containing less than five elevation values (i.e. less than 1/3)
are removed from the analysis, since their associated uncertainty (section 4.1.2) is not well determined. After down-sampling,
the comparability with the CS2 elevation data is increased, also in terms of the relative number of elevation data points from
the two satellite missions included in the analysis. IS2 observations constitute 73-76% of the total ice elevation measurements
used for generating the PRODEMs.

95   ### 2.3 ArcticDEM

We employ the ArcticDEM 500m gridded mosaic v3 (Porter et al., 2018) as reference DEM. ArcticDEM v3 is developed by
the Polar Geospatial Center, University of Minnesota, and it is constructed based on many thousand pairs of overlapping
optical stereo imagery (2m resolution) acquired over a multi-year period (2013-2017), the best of which have subsequently
been combined and down-sampled to form the ArcticDEM mosaic (Noh and Howat, 2015). The mosaic is constructed in tiles
100  of 100x100km, with each tile being registered to reference elevations using ICESat data, and subsequently blended at the edges
to match neighbouring tiles.

While the mosaic is based on very high-resolution elevation products, the associated mean elevations may not be representative
for the present-day snow-free summer ice-sheet topography. The individual DEM strips are acquired over many years, and in
105  different seasons, during which the surface topography has been continuously evolving. Hence, edge-matching by blending
and feathering of strips and tiles introduce artefacts in the final mosaic. Further, areas of low radiometric contrast, as well as
cloud cover and shadows, may introduce errors or data voids. Other error sources include slight misregistration of the stereo-
pairs, which may lead to large elevation errors in areas of high topographic variability when combining individual strips of
stereo imagery to a mosaic (PGC, n.d.).

110  ### 3 PRODEM data coverage

The PRODEMs are summer DEMs for the marginal areas of the Greenland Ice Sheet, including peripheral glaciers connected
to the ice sheet based on the BedMachine v5 ice cover mask (Morlighem et al., 2017, 2022). They are built entirely from
summer data (June 1st to September 30th), and the DEM coverage is limited to the outermost 50km wide band of the ice sheet
margin. This area encompasses most of the summer bare ice zone in recent years (Fausto and the PROMICE team, 2018). The
115  area and period are selected to ensure that the altimetry data primarily provides snow-free ice surface elevations. This is
required for compatibility between the CS2 and IS2 measurements, since the two satellite sensors differ in the way that they
interact with the surface: For snow-covered areas, the SIRAL radar signal may penetrate into the snow, whereas the penetration

depth of the ATLAS lidar is negligible. Combining the altimetry data from IS2 and CS2, we wish to eliminate as much as possible the effect of different snow penetration depths of the radar versus the laser signal.

120

To obtain PRODEMs for the marginal 50km of the ice sheet, we include satellite data from an extended area encompassing a 10km inland buffer zone to avoid edge effects in the DEMs. The satellite altimetry data are filtered to contain only measurements over ice-covered areas. With the collected data from CS2 and IS2 combined, the data coverage is sufficient to derive high-resolution annual maps of ice sheet topography in the marginal areas of the Greenland ice sheet. Using 500m grid

125    resolution, the interpolation distances from the nearest datapoint show a distribution with a mode in the 120-230m range, and a median of 454m (values for 2019 data; see Fig. 1a). Due to the denser satellite orbits towards the north, the interpolation distances tend to be slightly smaller there. Within any area, the data coverage is irregularly spaced, and the distribution of minimum interpolation distances is skewed towards high values, implying that, in a minority of cases, the accuracy of the interpolated elevations is significantly limited by data availability.

130

Figure 1b-d shows the 2019 data coverage in the regions around the three largest outlet glaciers from the Greenland Ice Sheet; Sermeq Kujalleq (Jakobshavn Isbræ), Kangerlussuaq Glacier and Helheim Glacier. The observations are distributed differently in other years. Lesser data density in some areas will be reflected as regions of increased uncertainty in the derived annual surface elevations for the given year.

135
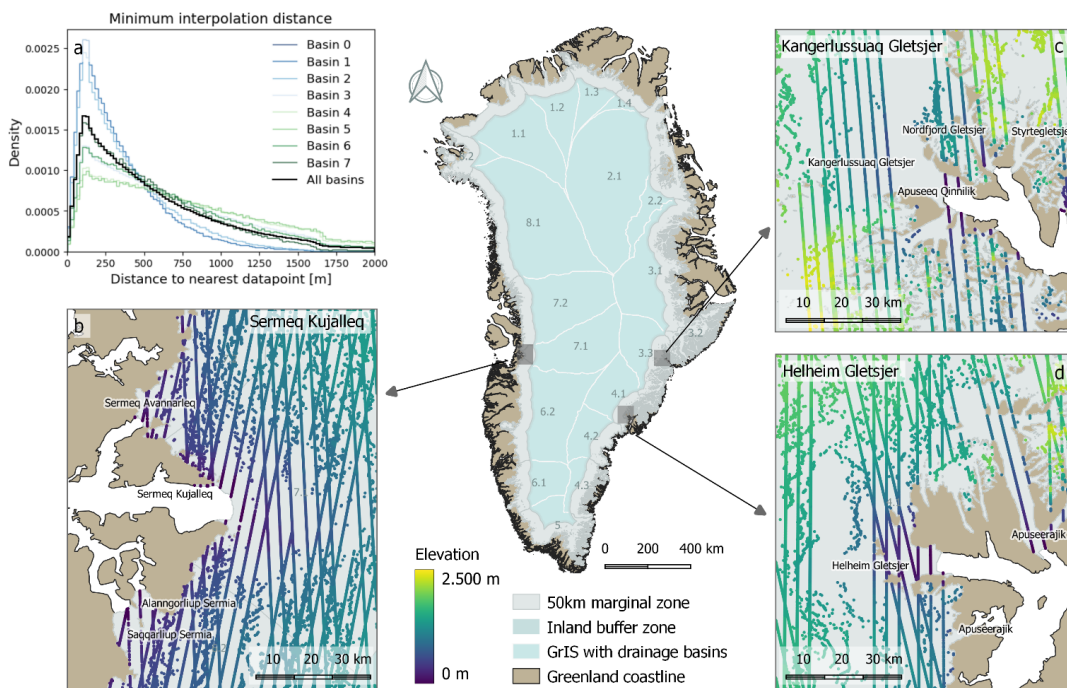
**Figur 1: a): Histogram showing the distribution of distances for each grid point to the closest data point (data from 2019). Distributions are shown for each main drainage basin (blue colours for drainage basins in North and East Greenland; green colours for basins in South and West Greenland; colour saturation is relative to basin latitude), and for the entire PRODEM area (black).**
140   **b-d): CS2 and IS2 data coverage for June through September 2019 over subsectors covering the area around the three largest outlet glaciers from the Greenland Ice Sheet: Sermeq Kujalleq (b), Kangerlussuaq (c) and Helheim Glaciers (d). IS2 data can be recognized as data acquired along straight lines, while CS2 data points are geolocated according to the POCA. For derivation of the PRODEMs, the ice sheet marginal zone was first divided up into subsectors using the drainage basin definitions from Zwally et al (2012), which are indicated with numbers on the overview map of the Greenland Ice Sheet. Official glacier names from (Bjørk et al., 2015).**

### 4 Estimating uncertainties and bias of the satellite altimetry data

#### 4.1 Observation uncertainties

During DEM construction based on the CS2 and IS2 satellite altimetry data, we include a measure for the uncertainty of the individual data points to inform on how much a given measurement should constrain the interpolated field. Proper uncertainty estimation is important: If uncertainties are overestimated, the resulting field will be too smooth, thus discarding much of the information existing within the observations. Conversely, if uncertainties are underestimated, the interpolation will tend to overfit the observations while inducing noise in the interpolated field.

This uncertainty should be understood as a measure of how well an observation represents the mean elevation field (spatial and timewise) at a given location. The degree to which a given observation represents the mean elevation field may be divided into four factors, which together constitute the total uncertainty:

$$\sigma_{tot}^2 = \sigma_{meas}^2 + \sigma_{geo}^2 + \sigma_{spatial}^2 + \sigma_{temp}^2 \tag{1}$$

Here, $\sigma_{meas}$ is the instrument measurement uncertainty, and $\sigma_{geo}$ is the elevation uncertainty caused by uncertainty in the geolocation of the observation. The spatial and temporal representability of an observation is captured in the latter two factors, $\sigma_{spatial}$ and $\sigma_{temp}$. Appropriate values for these two depend on the elevation field to be interpolated. For a 500-m resolution DEM, $\sigma_{spatial}$ is a measure of how well a given observation represents the average elevation field within a similar range, which depends on the spatial variability of the local elevation field. Further, the observations are gathered within a 4-month window, during which the surface elevation is changing over time, and the elevation field to be obtained is the mean elevation over an entire summer. The term $\sigma_{temp}$ indicates how well a given observation represents the mean summer elevation value at this location. The various uncertainty factors are combined in quadrature under the assumption that they are independent.

Given the different nature of the CS2 and IS2 observations, the primary factors affecting their uncertainty differ between the two data sets. We hence use different approaches to estimate representative values for the total observation uncertainty. The uncertainty models are constructed based on data from 2019. Since the measurement uncertainty is expected to be stable across years, we apply the resulting uncertainty model also for successive years.

#### 4.1.1 Uncertainty of the CS2 elevations

When operating in SARIn mode, the CS2 SIRAL radar system provides an integrated measurement of the surface elevation within the satellite footprint. The geolocation of the measurement (POCA) is associated with some uncertainty. This is primarily due to phase ambiguities, albeit the slope-induced errors associated with the SARIn data are much smaller than for conventional low-resolution mode radar altimetry (Hurkmans et al., 2012; Schröder et al., 2019). Yet, this issue is especially pronounced on smaller glaciers and ice caps as well as in the ice sheet marginal areas, such as those in this study, where the topographic relief may be significant (Levinsen et al., 2016; Wang et al., 2015).

To estimate the uncertainty associated with the CS2 observations, we perform an analysis of elevation differences for satellite track crossovers of the CS2 2019 summer data within our study area encompassing the marginal ice sheet zone. For each observation in a satellite track, the closest observation from another track within a 100m search radius is selected, and their associated elevations are compared. No limit on the allowed time difference is imposed. Part of the elevation differences is a result of actual surface fluctuations between the two measurement locations near to the crossing tracks caused by small-scale topographic variability, surface mass balance and/or dynamic changes taking place over the four-month summer period. This analysis provides an integrated assessment of the total uncertainty, since the derived elevation differences close to the cross-over locations may be due to either, or all, of the uncertainties.

A total of 38.079 crossings of CS2 satellite tracks exist within our study area during the summer of 2019. The resulting distribution of all CS2 elevation differences at the approximate cross-over locations is sharply peaked around 0 (Fig. 2a; grey histogram) with a median absolute deviation (MAD) of 1.1m. Various characteristics of the spread of the elevation difference

190   distribution may be used as an estimate for the uncertainty. MAD is a measure of dispersion, which, compared to e.g., the standard deviation, has the advantage of being more robust to outliers. It can be converted to an approximate Gaussian standard deviation ($s_{MAD}$) by multiplying with 1.4826. In the following, we will use $s_{MAD}$ as an approximate measure for the 1σ uncertainty of the CS2 observations.

195   It is not a very good approximation to apply a constant uncertainty value for all CS2 observations. Several factors are expected to cause a larger uncertainty in areas of sloping and/or rough terrain: The spatial representativeness for any given observation will be smaller, and an error caused by incorrect or slightly misplaced geolocation of the POCA will lead to a much larger error in the obtained elevation estimate.

200   We therefore investigate the relationship between local surface roughness and the dispersion of measured elevation difference distributions at approximate satellite track crossings. A map of the 100m-scale surface roughness is obtained from the ArcticDEM mosaic in 100m resolution, from which the roughness is computed as the largest elevation difference between the central pixel and its surrounding cells. We note that with this definition a flat sloping surface will have a roughness value depending on the slope. Binning the satellite crossings according to the local roughness, statistics for the distributions of

205   measured elevation differences are computed for different roughness values. The observations are divided into 50 bins, each containing a sufficiently large number (~600) of observations to obtain good estimates for $s_{MAD}$. A linear relationship exists between the logarithm to the local 100m-scale roughness and $s_{MAD}$ (Fig. 2b), while plateauing at a value of ~1m for low roughness values (log(roughness)<0). At these locations with little slope and surface irregularities, the observation uncertainty is primarily caused by measurement uncertainty and temporal variability, and this value (1m) may therefore be interpreted as

210   the uncertainty due to these factors only.
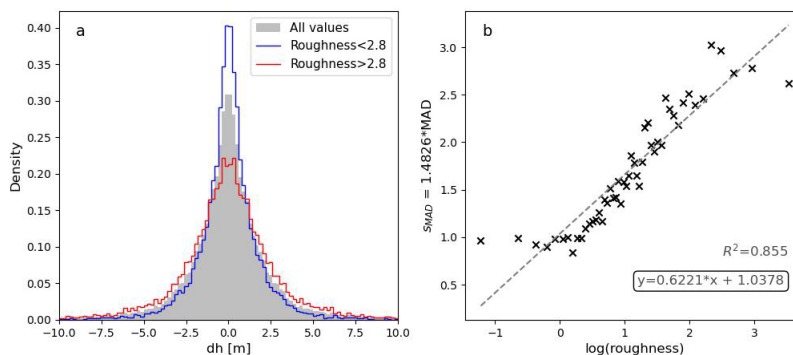
**Figure 2: a) Distribution of measured elevation differences (dh) at all satellite track near-cross-over locations within the study area (grey), and cross overs in areas with roughness higher (red) or lower (blue) than the median roughness value of 2.8, respectively. b) A linear relationship (dashed grey line) exists between the logarithm to the local 100m-scale roughness value and the dispersion of**
215   **the associated elevation difference distributions given in terms of $s_{MAD}$. Data from 2019.**

Spatial differences in CS2 observation uncertainty due to surface roughness are estimated accordingly: The logarithm to the local 100m-scale roughness is computed, and we apply the obtained linear relationship (Fig. 2b). Given the observed plateauing of the uncertainty for small surface roughness values, we further impose a minimum uncertainty value of 1m. The resulting distribution of uncertainty values for the CS2 observations within our study area in summer 2019 has a median value of 1.7m

220  (Fig. 3a; orange histogram). Reassuringly, this is very similar to the value of $s_{MAD}$ calculated based on all crossings in the study area ($s_{MAD} = 1.4826 * 1.1\text{m} = 1.6\text{m}$).

Lastly, it should be noted that the CS2 observations are inherently biased towards higher elevation values: Since the elevation estimates from CS2 are associated with the POCA within the satellite footprint, CS2 will preferentially sample the topographic

225  highpoints rather than topographic lows located within the satellite footprint. This inherent bias of the CS2 elevations is not accounted for. One consequence of this measurement bias is that the measured elevation differences obtained close to a crossover of satellite tracks may not reflect the full variability of the terrain over small distances. This will result in an underestimation of the observation uncertainty due to spatial variability, particularly in highly irregular terrain.
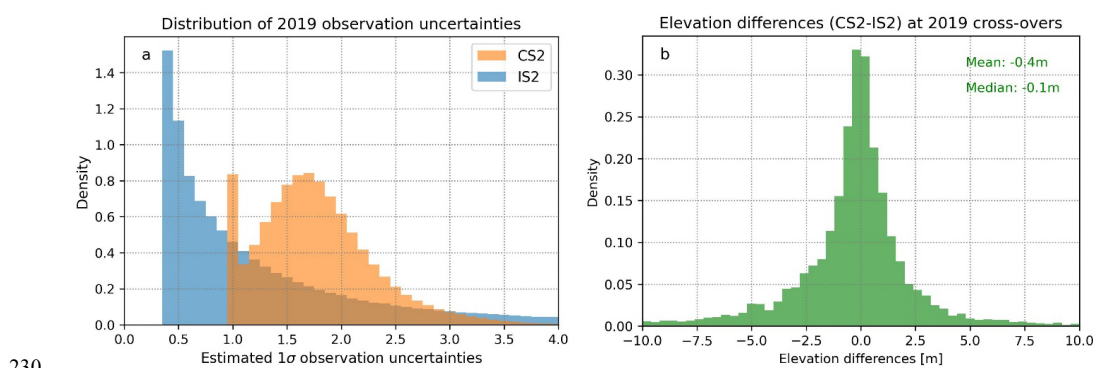
230

**Figure 3: a) Distribution of derived total uncertainties for the summer 2019 CS2 (orange) and IS2 (blue) altimetry data, respectively. b) Distribution of elevation differences, computed as $dh = h_{cs2} - h_{is2}$, near cross-overs of CS2 and IS2 satellite tracks, when imposing relatively strict limits in terms of maximum distance and time between acquisitions. Data from the PRODEM area for summer 2019.**

235  **4.1.2 Uncertainty of the IS2 elevations**

The measurement precision of the IS2 ATL06 product has been documented to be as small as 9cm over the interior part of Antarctica (Brunt et al., 2019), and, compared to CS2, the ATLAS instrument provides much better resolved and localized elevation data with no topographic preference (Magruder et al., 2020). We note that beginning 24 October 2021, the ATL06 V5 data set contains a geolocation error with a mean across-track position error of 1.5m (up to 8m), but on average the resulting

240  height errors are small (<1 cm) (NSIDC, 2023). Hence, apart from outliers due to occasional errors in the ATL06 data caused by errors in tracking the surface within the photon cloud, the total observation uncertainty (Eq. 1) is dominated by the spatial and temporal variability of the surface elevation relative to the mean elevation field ($\sigma_{spatial}, \sigma_{temp}$).

By construction, the 250m-median-averaged IS2 data used for DEM construction (section 2.2) already includes spatial

245  averaging in the along-track dimension. However, spatial representability of the along-track-averaged values depends on the local topography; the precise location of the track will influence the resulting average more in areas of high topographic relief. We estimate the uncertainty contribution from spatial representability for each data point individually based on the local variability of the original higher-resolution ATL06 data set: Within each 250m segment of the IS2 tracks, the along-track small-scale topographic variability is computed as $s_{MAD}$ of the elevation distribution of the ATL06 20m resolution data. We

250  use these values to approximate a 1σ uncertainty of the IS2 observations due to spatial variability of the elevation field. The derived uncertainties display large spatial variability strongly correlated with surface roughness, and consequently much larger uncertainty values towards the margin where the topography tends to be substantially rougher than in the smooth inner areas of the ice sheet.

255    To investigate how well the average IS2 observation represents the mean summer elevation field ($\sigma_{temp}$), we again analyse the observed elevation differences of measurements located close to satellite track crossings during summer 2019. Compared to CS2, this results in a more strongly peaked distribution of elevation differences, with a corresponding dispersion of $s_{MAD} = 1.1$m. Desiring to eliminate as much as possible the effect of spatial variability, we impose increasingly restrictive limits for the maximum distance allowed between the observations to be compared. Based on a total of 57541 cross-over locations (when

260    applying a maximum distance of 100m), we find a linear relationship between the allowed maximum distance and the spread of the elevation difference distribution. Extending the linear trend towards zero, the distribution is expected to have a spread of $s_{MAD} \approx 0.4$m when the observations to be compared are measured at the same location. This value reflects the average surface variability throughout the summer. We hence set $\sigma_{temp} = 0.4$m and include this as a measure for the uncertainty caused by dynamic changes in surface elevation over the four-month observational period. This term is assumed spatially

265    constant, and it is added in quadrature to the uncertainties caused by surface topography to obtain a measure for the total uncertainty of the individual IS2 datapoints.

The distribution of the individually estimated IS2 total uncertainties in 2019 (Fig. 3a; blue histogram) has a median of 1.0m. We also here note the similarity of the obtained median uncertainty value to the value of $s_{MAD}$ (1.1m) calculated based on all

270    IS2 crossings in the study area during this year.

**4.2 Bias estimation**

As previously mentioned, we expect a disparity between elevation measurements obtained from CS2 and IS2 in presence of snow. This may give rise to biases, in which case these must be corrected prior to combining elevation data from the two satellites. The PRODEMs, however, are constructed based on elevation data from the ice-sheet marginal areas during summer,

275    where the snow cover is limited, likely resulting in small biases only. This assumption is verified by an analysis of IS2 versus CS2 height observations, while imposing restrictive limits of a maximum distance of 100m and a maximum time difference of two weeks. We find no evident bias between the elevation estimates obtained from the two satellite sensors: Based on all 6194 crossovers in 2019 fulfilling these criteria, the elevation differences are found to be distributed with a median value close to zero (-0.1m, Fig. 3b). The negative value implies that CS2 elevations overall tend to be slightly lower than the IS2 elevations.

280    This bias, however, shows substantial spatial variability, with the median elevation difference attaining both negative and positive values depending on drainage basin. Apart from the effects of new and old snow lingering on the ground, part of these differences is likely caused by the topographic preference of CS2 towards measuring high elevation points, which will appear as a positive elevation bias of the CS2 data. In general, the elevation differences are well within the uncertainties of the CS2 data points, and we hence conclude that, within the associated uncertainties, we do not observe any significant bias.

285    **5 Constructing the PRODEMs**

**5.1 Regional PRODEMs for marginal drainage basin subsectors**

For computational purposes, we create regional PRODEMs for marginal subsectors based on drainage basin outlines, which are subsequently combined to form a full-margin DEM. We use the drainage basin definitions from Zwally et al. (2012), which divide the Greenland ice sheet into 19 drainage basins (Fig. 1). For each sub-sector DEM, data from a 10km neighbourhood is

290    included to avoid artefacts around drainage basin edges.

### 5.2 Elevation anomalies relative to ArcticDEM

Prior to interpolation, the satellite altimetry data are detrended by subtracting a reference DEM (ArcticDEM) from each altimetry point measurement using linear interpolation. A few areas within the PRODEM region are not covered by data in the ArcticDEM mosaic, and an interpolated surface is used as reference here. The PRODEMs are constructed using the same coordinate system (EPSG:3413) and grid as the ArcticDEM 500m mosaic, thus avoiding additional interpolation when later adding the interpolated elevation anomalies to the reference DEM.

Based on the map of observed elevation anomalies relative to ArcticDEM, some outliers in the altimetry data are clearly identifiable. To clean the data, we successively apply a 10x10km spatial filter to the elevation anomaly data, and observations outside the 5σ range of local variability are identified as outliers and removed. The filtering is repeated 10 times, after which no or few outliers are detected. During the construction of PRODEM19, a total of 3.0% of the CS2 data and 0.2% of the IS2 data (together constituting 0.9% of all data) are flagged as outliers. Further investigations show that many IS2 observations flagged as outliers are likely not measurement errors. The vast majority of these are located next to a nunatak, and the irregularity in elevation anomalies in these areas, as picked up by the spatial filter, is caused by large variability in the reference field obtained by linear interpolation of the 500m-resolution ArcticDEM to the measurement locations. We therefore attribute this perceived irregularity to errors and resolution issues in the ArcticDEM mosaic (see discussion). Including these data would, however, give rise to spatial discontinuity in the elevation anomalies, which is unfavourable for interpolation. In contrast, the CS2 observations flagged as outliers are evenly distributed throughout the study area, suggesting that these indeed represent inaccurate altimetry measurements.

### 5.3 Spatial interpolation of the elevation anomaly field

The PRODEMs are spatially interpolated from the satellite altimetry point measurements by Ordinary Kriging. In essence, kriging performs an optimal prediction of a continuous field by exploiting knowledge of the spatial covariance of the field (see e.g. Hengl (2009)). The spatial covariance is specified in terms of a variogram, which can be extracted from the point cloud, and this information is subsequently used to assign distance-dependent weights to nearby data points. Several Kriging variants exist. In Ordinary Kriging, the predictions are formed as the sum of a (locally) constant function and a spatially correlated stochastic field. Kriging can account for variable uncertainty of individual data points during the interpolation, and it is a widely used method to interpolate geophysical fields (e.g. (Bamber et al., 2001; MacGregor et al., 2015; Bales et al., 2001)).

Kriging relies on the data to be isotropic (i.e. have non-directional properties) and stationary (i.e. have a constant mean field and variance) so that the spatial covariance structure is representative across the study space. While it is reasonable to assume an elevation field to be isotropic, neither the ice surface elevation field, nor the elevation anomaly field relative to ArcticDEM, are stationary. Surface elevations strongly violate the stationarity requirements, with mean elevations decreasing considerably towards the ice sheet margin. The elevation anomalies do not show a similar trend, and we apply the Kriging algorithm to this transformed data set. For neither data set, however, the field variance is stable across space: Both the elevation and the elevation anomaly fields generally display higher variance in the topographically rough areas near the ice sheet margin than in the smoother inland areas.

Consequently, the spatial covariance of the elevation anomaly field relative to ArcticDEM cannot be properly described by a single variogram. To account for this, we first estimate annual maps of the variogram parameters describing the varying spatial correlation structure of the elevation anomalies across the PRODEM area (section 5.3.1). For a given location in the PRODEM grid, an appropriate set of variogram parameters is subsequently extracted and applied in the kriging routine (section 5.3.2) to

produce an interpolated value for the elevation anomaly. The final PRODEM is constructed by adding the map of derived elevation anomalies to the ArcticDEM mosaic, thereby forming an updated summer DEM for the region.

### 5.3.1 Modelling the regionally varying spatial covariance structure

335 We first assess the varying spatial covariance structure of the elevation anomalies across the 50km marginal ice sheet zone forming the PRODEM area. From the point cloud of elevation anomalies, we observe that substantial changes in field characteristics sometimes take place over small spatial scales (<5km). Such rapid change occurs e.g., in regions where a smooth low-elevation outlet glacier is surrounded by higher elevation ice-covered mountainous areas, with the latter region displaying substantially higher spatial variability also in the elevation anomalies.

340

Spatial covariance may be represented by a variogram, which is a measure of half the variance of the differences in field value at two locations as function of the distance ("lag") between those locations. To account for the spatially varying covariance structure of the elevation anomaly field, individual variograms are constructed for points in a 10km grid covering the PRODEM area. The experimental variograms are computed with the GSTools package using the Cressie estimator (Müller et al., 2022;

345 Cressie, 1993), which is relatively robust to outliers. Each variogram is based on the nearest 5000 observations within a 50km radius of the grid point, the first condition generally being the most restrictive (mean distance to the observation furthest away is 32km). We use 500m binning of distance lags and a maximum bin size of 15km, which provide sufficient data points for consistent retrieval of the variogram at all lags.

350 The experimental variograms are subsequently modelled using the Matérn covariance function with smoothness parameter 3/2 (Stein, 1999). This is a widely used covariance model suitable for spatial variables with moderate smoothness. The covariance function is given as the product of a linear and an exponential function (Eq. 2), allowing it to represent diverse behaviours at short lags:

$$C(d) = \sigma^2 \left(1 + \frac{\sqrt{3}d}{\rho}\right) exp\left(\frac{-\sqrt{3}d}{\rho}\right) \tag{2}$$

355 Here, $C(d)$ is the covariance between two points separated by distance $d$, $\sigma^2$ is the variance of the field, and $\rho$ is a length scale parameter for the covariance function. The latter is a measure for how far an observation carries information on the surrounding field; the covariance of two points spaced with a distance of $\rho$ is approximately half the field variance. We define the effective range, $L_e$, as the distance after which two data points are essentially no longer correlated (covariance has decreased by 95%), which can be calculated as $L_e \approx 2.7\rho$. For infinitesimal separation distances, a nugget effect ($\sigma_n^2$) may be added to the

360 covariance function. The nugget represents measurement errors and/or micro-scale variability in the data, e.g., natural variability at scales smaller than the sampling distance, both of which will cause two measurements at essentially the same location to differ slightly. Adding a nugget effect, a model for the variogram, $\gamma(d)$, can be obtained from the covariance function by (see Hengl (2009)):

$$\gamma(d) = \sigma^2 + \sigma_n^2 - C(d) \tag{3}$$

365 Given its flexible structure, the Matérn covariance model provides a good description of the various covariance structures existing within the elevation anomaly field.

A Matérn variogram model is fitted using robust least squares to each of the variograms in the coarse-resolution grid across the PRODEM area. The length scale, $\rho$, is constrained to the interval 500m to 20km (effective range: 1.4-54.0km). No bounds

370 are imposed for the remaining two parameters. Given the high density of altimetry observations, the predicted field values will tend to be dominated by a large number of nearby observations carrying high weights in the interpolation, and it is therefore most important to correctly capture the covariance structure at close distances (e.g., small lags). To ensure that the fitted

variogram models are well representing the covariance at small lags, these are weighted higher in the fitting procedure: Applied weights are inversely related to the lag value of the empirical variogram and decrease to 50% at 5km. Figure 4e shows four

375    examples of representative experimental variograms and fitted variogram models. The procedure is repeated for each year in the PRODEM series. In the following, we focus on the variogram parameter fields obtained from summer 2019 data, but the overall patterns are consistent across the four-year period covered by the current PRODEM series.

To avoid discontinuities in the final PRODEMs, the variogram parameter fields must be spatially continuous. Continuity of

380    the variogram parameters is also expected since adjacent models are based on partly the same data set; the variograms are obtained for each point in the 10km grid, with each based on observations within a 50km radius. At a few locations, it is not possible to obtain a good fit to a Mátern variogram (low $R^2$-score of the fit; see the map of retrieved $R^2$-scores for PRODEM19 in Fig. 4d), and these places can often be identified as outliers in the variogram parameter fields. To eliminate these, we remove retrieved parameter values associated with low $R^2$-scores (defined as the lower 5% percentile of the observed distribution of

385    $R^2$ values; this value being ~0.6 for all years). Subsequently, the parameter fields are smoothed using a 3x3 pixel (i.e., 30x30km) spatial mean filter. Smoothed values are also utilized for filling in parameter values at locations where the fitting procedure did not result in a good fit.
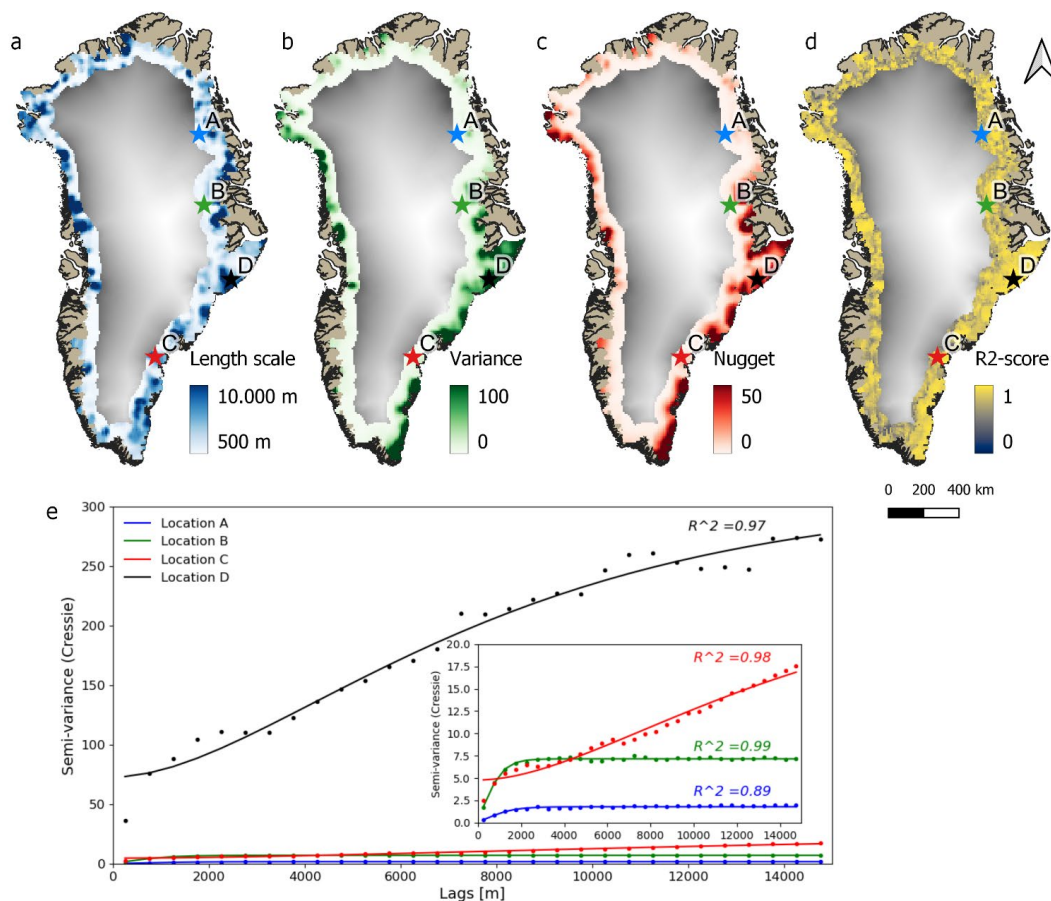
**Figure 4: a, b, c)** Spatial variability across the PRODEM area of the three parameters of the Matérn variogram model with

390    smoothness parameter 3/2; the length scale (a), variance (b) and nugget (c), respectively. The filtered parameters fields for 2019 data are shown. ArcticDEM elevations (grey) are used for background. **d)** $R^2$ score (Pearson correlation coefficient) of the model fit to the experimental variograms across the area. A value of $R^2$ close to 1 signifies a good fit. **e)** Four representative experimental and fitted variogram models for different sets of model parameter values found within the PRODEM area; locations of the four variograms are indicated with letters A-D in the maps (a-d).

395

The large-scale patterns of variogram parameters (Fig. 4a-c) reflect the differences in spatial covariance across the marginal ice sheet zone. Elevation anomalies in the innermost part of the marginal zone are generally characterized by smooth fields, with low variance and small nugget values (Fig. 4, location A), implying that the elevation anomaly in these areas is very well-characterized by nearby observations. The variograms here tend to display small length scales, reflecting that local peaks and

400 valleys exist within the otherwise smooth anomaly field. Moving towards the margin, the variograms gradually change towards higher variance and nugget values, but the length scale remains small (Fig. 4, location B). Upstream outlet glaciers, we observe a varying pattern of high variance and nugget values, often combined with large length scales (Fig. 4, locations C and D). Particularly East Greenland outlet glaciers tend to be characterized by extremely high variance and nugget values (location D).

405 For each PRODEM 500m grid cell, an appropriate set of variogram model parameters is found by bilinear interpolation in the coarser parameter grid, and these are used as input to the kriging routine.

### 5.3.2 Interpolated fields of elevation anomalies and associated uncertainty

For each grid point, the Ordinary Kriging interpolation is based on up to 200 nearby observations. The input data, however, are not distributed evenly, particularly given the closely spaced IS2 observations obtained along straight lines. To ensure that

410 data included in the interpolation are well distributed around the grid point, these data are selected by dividing the neighbourhood around the grid point into 8 subsectors and using the nearest 25 observations from within each subsector.

The expected field value at location $x_0$, $\hat{f}(x_0)$, can be calculated by weighting the surrounding $J$ observations $(x_i, z_i)$ according to their distance to $x_0$ using the local variogram function:

415 $$\hat{f}(x_0) = \mu + \lambda_0^T \cdot (z - \mu) \tag{4}$$

Here, $z$ is a vector with the field observations, and $\lambda_0$ is a vector containing the weights for these at location $x_0$. We apply the local median of the observations as a robust estimator for the local mean value, $\mu$, of the elevation anomaly field. The weights can be calculated by the following matrix equation (see Paciorek (2008)):

$$\lambda_0 = (C + N)^{-1} c_0,$$

420 where $C$ is the covariance matrix between the $J$ observations calculated based on their pair-wise distance using the local variogram parameters (Eq. 2), and $c_0$ is a vector for the covariance of the field at location $x_0$ and the various $x_i$. The total measurement noise and micro-scale variability for each observation is represented by the noise matrix $N$. This is a diagonal matrix whose entries on the diagonal are the squared observation uncertainties, i.e., $N = \tau\tau^T$, with $\tau$ being the vector of observation uncertainties. We set the uncertainties to be the observation error of the individual observations or the nugget

425 value of the variogram, whichever is higher. To ensure that the weights sum to 1, an extra row and column is added to the kriging matrix equation, where $w_0$ now are the final kriging weights, and $\varphi$ is the so-called Lagrange multiplier (Hengl, 2009):

$$\lambda_0' = \begin{bmatrix} w_0 \\ \varphi \end{bmatrix} = \begin{bmatrix} C + N & 1 \\ 1^T & 0 \end{bmatrix}^{-1} \begin{bmatrix} c_0 \\ 1 \end{bmatrix}$$

We also estimate the prediction uncertainty of the interpolated elevation anomaly field. The uncertainty primarily depends on

430 the distance to (and uncertainty of) the nearest data points, along with the covariance structure informing on how much the field is correlated at those distances. Two kinds of uncertainties may be computed: The uncertainty of the underlying field value, and the predictability of new data points obtained at the same location. The latter also accounts for the uncertainty associated with the micro-scale variability of the field and measurement uncertainties. The variance associated with the interpolated elevation anomaly field at location $x_0$ can be estimated as the weighted average of covariances between $x_0$ and

435 all observation points $x_i$:

$$\mathrm{var}[\hat{f}(x_o)] = \sigma^2 - c_0^T \cdot w_0 \tag{5}$$

with $\sigma^2$ being the local variance of the field, as determined from the local variogram. To estimate the variance of new observations $z_0$ obtained at the same location $x_0$, also the observation uncertainty must be addressed, and an extra term is added to the equation (Paciorek, 2008):

440 $$\mathrm{var}[\hat{z}(x_o)] = \mathrm{var}[\hat{f}(x_o)] + \tau^2 \tag{6}$$

This is the uncertainty to be used for validating the resulting DEM (section 7).

Applying the above equations using the previously determined spatially varying variogram parameters, we derive estimates for interpolated elevation anomalies (Eq. 4) and associated field variances (Eq. 5) at all PRODEM grid centre points. To
445 improve the estimation of the mean elevation anomaly across the grid cell, we subsequently smooth the field by applying a 3x3 grid cell mean filter on the elevation anomalies obtained for grid cell centres. The resulting anomaly field and associated uncertainty is shown in Figure 5a-b. For each grid point, we also apply Eq. 4 to derive the weighted average acquisition time of observations (in units of day-of-year) used in the elevation prediction (Fig. 5c). This provides an assessment of the average day during the four-month summer period that the local interpolated elevation surface is most representative of, thereby
450 providing a time stamp with each pixel in the DEM.

Finally, the ArcticDEM mosaic is added to the obtained elevation anomaly field, forming an annual summer PRODEM for the marginal ice sheet zone (Fig. 5d). In a few places, the interpolated anomalies give rise to negative elevation values, which is unrealistic. This is caused by boundary effects; limited data leads to a retrieved constant dh-field in an area close to the margin
455 where ArcticDEM displays large variability. For these few areas, we correct the PRODEMs accordingly.
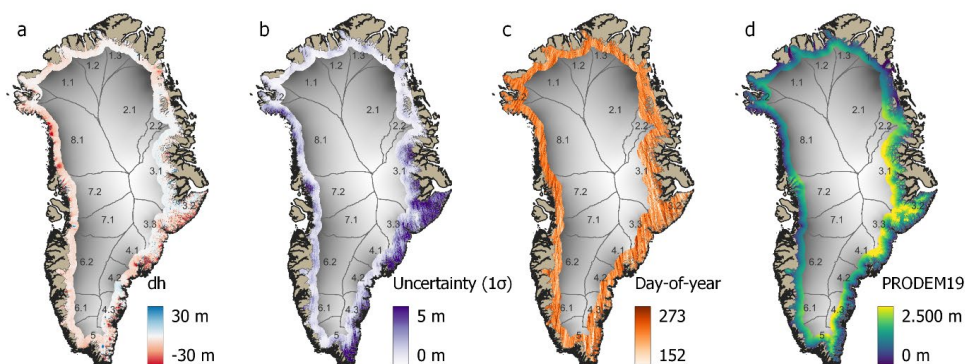
**Figure 5: PRODEM19 results. a) The resulting field elevation anomalies (dh) relative to ArcticDEM, along with b) the associated uncertainty (1σ) on the interpolated field, c) the weighted day-of-year of the interpolated surface, going from June 1st (day: 152) to September 30th (day: 273), and d) the resulting PRODEM19 elevations. ArcticDEM elevations (grey) are used for background, with**
460 **drainage basins indicated.**

## 6 General attributes of the PRODEM series (2019-22)

Figure 6 shows the distributions of PRODEM19 elevation anomalies relative to ArcticDEM (Fig. 6a), uncertainty of the interpolated elevation fields (Fig. 6b), and the associated time stamp of the derived surfaces (Fig. 6c). Distributions are shown for the entire PRODEM area as well as for each major drainage basin. Over the current four-year PRODEM period, the various
465 distributions evolve, but the dominant patterns persist (Fig. 7).

The distribution of elevation anomalies (Fig. 6a) is distinctly leaning towards negative values (i.e., implying a general lowering of the surface) with a median value for the entire PRODEM area of -2.7m (2019 values), which is much larger than the

PRODEM uncertainties. We attribute this to an actual surface lowering of the ice sheet that have taken place since the acquisition period (2013-2017) of the stereo imagery utilized for generating ArcticDEM. The spread of the distribution of elevation anomalies is large, however, and with an extended tail towards negative values. Spatially, negative anomalies (decreased elevations) dominate the West Greenland marginal areas (Fig. 6a; green curves), while regions with positive anomalies (increased elevations) are primarily located in East Greenland (Fig. 6a; blue curves), as it can also be seen from Figure 5a. For all drainage basins, however, the median elevation anomaly is negative.
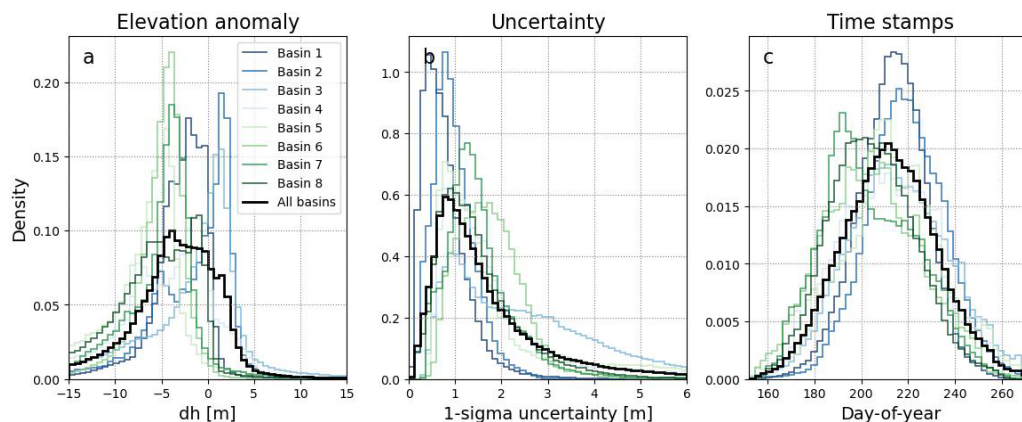
**Figure 6: Distribution of a) PRODEM19 elevation anomalies to ArcticDEM, b) uncertainties on the PRODEM19 elevation field, and c) weighted day-of-year of the altimetry observations used as input for the interpolation. Histograms are shown for the entire PRODEM area (black lines) as well as individually for all major drainage basins, with blue colours for drainage basins in North and East Greenland, and green colours for basins in South and West Greenland. Colour saturation is relative to basin latitude.**

The overall spatial pattern is stable over time (Fig. 7): The median elevation anomaly for each basin only shows minor changes over the four-year PRODEM period, with the difference between values for individual drainage basins being much larger than the change over time within a single basin. For most basins, the elevation anomalies trend towards slightly more negative values over time, indicative of overall decreasing elevations, and the median of elevation anomalies across the entire PRODEM area show a steady decrease.
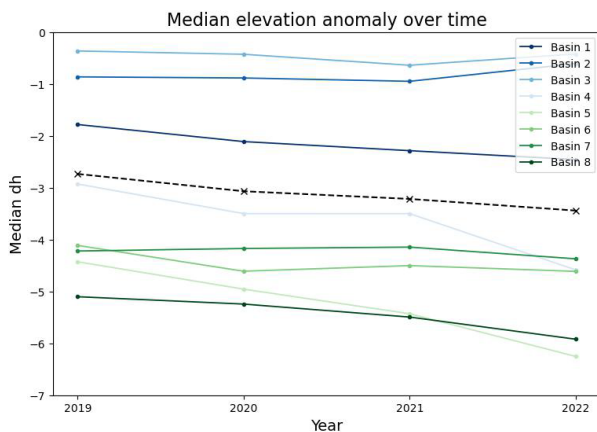
**Figure 7: Evolution in median elevation anomaly relative to ArcticDEM over the four-year PRODEM period 2019-2022. Values are given both on drainage-basin scale (coloured from blue to green, with blue being marginal drainage basins in North and East Greenland, and green being basins along the South and West Greenland coast; darker colours correspond to higher latitudes), and for the entire PRODEM area (black dotted line).**

Areas with poor data availability are reflected by increased uncertainties of the interpolated surface. The median 1σ uncertainty of the PRODEM19 elevation anomaly field, and hence also the PRODEM19 elevations, is 1.4m (Fig. 6b). Similar values are

495 obtained for subsequent years. However, the distribution has an extended tail towards higher values, implying that some areas cannot be interpolated very accurately based on the available data. For all years, this is particularly an issue for drainage basin 3, for which an exceptionally long tail exists, corresponding to an extended area of relatively large uncertainties. Given denser data close to the pole due to the satellite orbits, the uncertainty generally decreases towards the north.

## 7 Validation of the PRODEMs

500 ### 7.1 Leave-one-out cross-validation

As independent validation data are sparse, we assess the robustness of the PRODEMs using leave-one-out cross-validation: A subset of observations is removed, and based on the reduced data set, we predict the elevation at the location of the removed data points to evaluate the prediction error. This method allows reliable validation with good spatial distribution across the entire PRODEM area, and it provides robust estimates of the product performance with respect to the input data.

505

The subset of removed data points consists either of one track of CS2 data or IS2 data (one track consisting of all three strong beams), as these may be correlated. Due to computational limitations, we refrain from performing a full analysis, in which this process should be repeated on subsets consisting of all tracks independently and limit the number of repetitions to maximum 50 times for each basin, after which the results are found to stabilize. On average one track of removed data corresponds to

510 0.5% (CS2) and 1.9% (IS2) of the total data set within a basin. The prediction errors are subsequently normalized relative to the predicted standard deviation of new observations obtained at the given locations (Eq. 6). If elevations are well estimated within their associated uncertainties, the normalized prediction errors should be distributed according to the standard normal distribution.
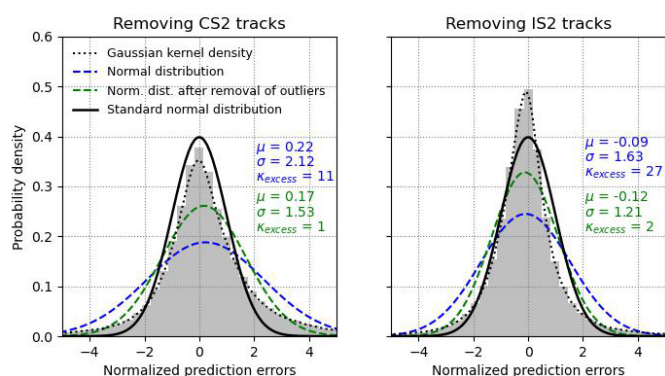
515 **Figure 8: Distribution of PRODEM19 prediction errors of the elevation anomaly relative to the estimated 1σ uncertainty of the interpolated field after removal of either a) one track of CS2 data, or b) one track (consisting of three beams) of IS2 data. For both distributions are shown the associated normal distribution based on calculating the mean and standard deviation of the prediction errors (blue) and after removal of outliers (defined as normalized errors outside ±5) (green), and the probability distribution using a Gaussian kernel density estimate on the data (dotted black line). The standard normal distribution (solid black line) is shown for**
520 **comparison.**

Figure 8 shows the normalized prediction error distributions for PRODEM19 after successive removal with resampling of one track of CS2 and IS2 data, respectively, within each drainage basin. Both sets of normalized prediction errors are reasonably well described by the standard normal distribution. Similar results are obtained for subsequent years in the PRODEM series (Table 1), and on average 56% (CS2) and 69% (IS2) of the predicted elevations fall within their associated 1σ uncertainty

525   interval. The slight deviation of the central distribution of CS2 prediction errors from the theoretically expected value (68%) may partly be attributed to uncertainties in the CS2 validation data, which are not considered in this analysis. All distributions display higher central peaks (higher kurtosis) than that of a normal distribution, and this is especially prominent for the analysis of prediction errors validated against IS2 data. It indicates that outliers in normalized prediction errors (e.g., errors in elevation estimate substantially larger than the prediction uncertainty) are more likely than theoretically expected, but also that most

530   normalized prediction errors are clustered around zero. For removal of IS2 tracks, this results in most elevation estimates having errors smaller than their associated uncertainty. We note that depending on which data set is partly removed and used for validation, there is a tendency towards a slight overestimation (CS2) or underestimation (IS2) of the observed elevations. This feature is robust across years and drainage basins, albeit with large regional differences in magnitude, and it is likely due to the construction of the PRODEMs from two sensors that interact differently with the surface.

535

| Distribution of normalized prediction errors | | 2019 | 2020 | 2021 | 2022 |
|---|---|---|---|---|---|
| CS2 | $\mu$ | 0.22 (0.17) | 0.19 (0.17) | 0.22 (0.19) | 0.20 (0.17) |
| | $\sigma$ | 2.1 (1.5) | 2.1 (1.5) | 2.2 (1.5) | 2.2 (1.5) |
| | $\kappa_{excess}$ | 11 (1) | 10 (1) | 33 (1) | 79 (1) |
| | Within standard central region ($\pm 1$) | 56% | 57% | 56% | 56% |
| IS2 | $\mu$ | -0.09 (-0.12) | -0.05 (-0.08) | -0.08 (-0.10) | -0.04 (-0.09) |
| | $\sigma$ | 1.6 (1.2) | 1.6 (1.2) | 1.6 (1.2) | 1.6 (1.2) |
| | $\kappa_{excess}$ | 27 (2) | 26 (3) | 35 (3) | 36 (3) |
| | Within standard central region ($\pm 1$) | 68% | 70% | 69% | 70% |

**Table 1: Parameters describing the distribution of normalized prediction errors after cross-validation based on successive removal with replacement of one track of CS2 or IS2 data, respectively, for each year in the current PRODEM series. In the ideal case, the normalized prediction errors should form a standard normal distribution, e.g., mean value ($\mu$) equal to 0, standard deviation ($\sigma$) equal to 1, excess kurtosis ($\kappa_{excess}$) of 0, and with 68% of the data falling within $\pm 1$ (central region with $\sigma = 1$) of the distribution.**
540   **For both satellites and all years, the distribution of normalized prediction errors shows good consistency with these values. Values in parentheses are computed after removal of extreme outliers (defined as values outside $\pm 5\sigma$, with $\sigma = 1$ as for the standard normal distribution).**

In summary, the prediction errors of the elevation fields are generally well distributed according to the prediction uncertainty. Since uncertainties in the validation data are not considered in this analysis, we consider the prediction errors based on

545   validation against the more accurate IS2 data to better reflect the elevation field uncertainties. We hence conclude that the PRODEMs within their associated uncertainties provide a good description of the true elevation fields. In most places, the estimated uncertainties are even somewhat conservative, however locations with very large errors in interpolated elevations are more frequent than theoretically predicted. Parts of this discrepancy may be due to the observations being acquired at different times during the summer, during which the surface elevation may change non-negligibly due to surface mass balance

550   processes.

**7.2 Comparison to an IS2-only Greenland DEM obtained for the period 2018-19**

Very few large-scale DEMs exist for the Greenland ice sheet that is valid for the PRODEM period. The exception is a newly developed DEM derived from IS2 data from November 2018 to November 2019 (in the following abbreviated IS2DEM19), developed based on a spatiotemporal fitting model (Fan et al., 2022).

555

For several reasons we do not expect the IS2DEM19 to be identical to PRODEM19. A significant difference is that IS2DEM is based on data from an entire year, during which the surface elevations evolve with the seasons. A larger snowpack during

the winter season is expected to result in generally higher elevations in IS2DEM19 than in PRODEM19. This is corroborated by a comparison of the two elevation fields; their median elevation difference across the marginal ice sheet zone is -1.9m, with

560    the negative sign indicating that PRODEM19 tends to display lower elevations.

Further, the PRODEMs are derived as elevation anomalies to ArcticDEM, whereas such an approach has not been taken for IS2DEM19. Looking at the small-scale features of the DEMs, this difference in approach becomes evident, with many of the fine-scale features existing in ArcticDEM being preserved in the PRODEM elevations (albeit in a modified form according to

565    the relatively smooth elevation anomaly field). An example of how the fine-scale structure differs for the two DEMs is shown for Petermann Gletsjer in Northern Greenland in Figure 9, along with a comparison to ArcticDEM. The structure of PRODEM19 is fairly similar to that of ArcticDEM, whereas its large-scale field is more similar to IS2DEM19. This is especially evident for an area in the outer part of the glacier tongue, where both PRODEM19 and IS2DEM19 display substantially higher elevations than ArcticDEM. This increased resolution of fine-scale features in the PRODEMs comes at

570    the cost, however, of additional assumptions regarding the stability over time of the small-scale structure of the elevation field.
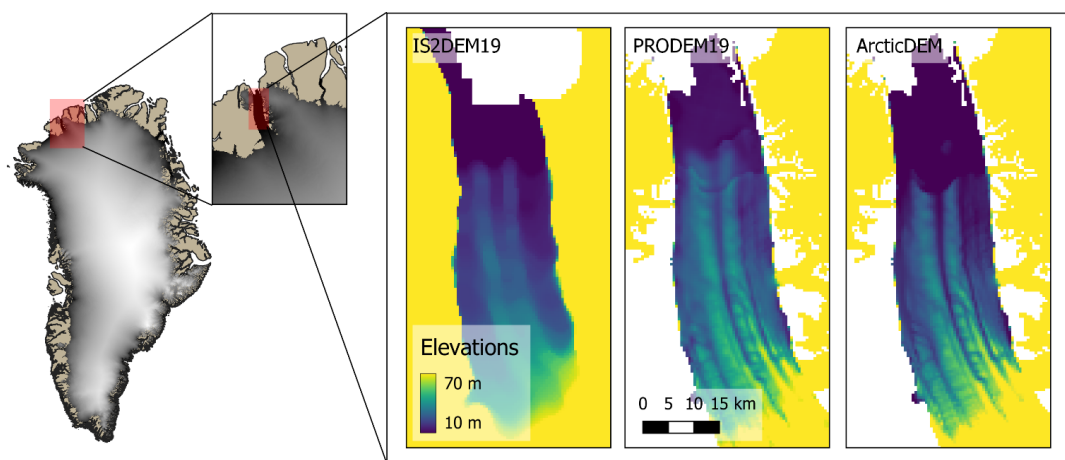
**Figure 9: A comparison of the three elevation fields: IS2DEM19, PRODEM19, and ArcticDEM across Petermann Gletsjer. Coverage of the three DEMs varies slightly across the region.**

575    **9 Discussion**

For reliable outcome of kriging, the field to be interpolated must be quasi-stationary, and hence it is a prerequisite to use a reference DEM to produce elevation anomalies. Our approach has the added advantage of inheriting the detailed elevation from ArcticDEM to maintain the high resolution of the PRODEMs also in areas poorly covered by the satellite altimetry data. However, artefacts in the reference DEM may be carried over to the updated DEM, and thus high quality of the employed

580    reference DEM is vital.

Despite the high quality of ArcticDEM also this DEM has issues, and some of these are apparent in the interpolated elevation anomaly fields. Due to ArcticDEM being constructed as a mosaic of 100x100km tiles, with each tile registered to ICESat reference elevations, our elevation anomalies display a checkerboard pattern with each tile having a slightly different mean

585    value. Perhaps most strikingly, this is the case for an area in Southeast Greenland (Fig. 10), where the distribution of anomalies in the northernmost tile (Fig. 10, tile a) is -6.1m ± 3.3m, whereas the distribution in the adjacent southernmost tile (Fig 10, tile b) is 3.2m ± 2.6m (PRODEM19 values). This issue must be kept in mind when discussing the derived field of elevation

anomalies to ArcticDEM, and we emphasize that absolute values of elevation anomalies for individual glaciers should only be compared with caution.

590
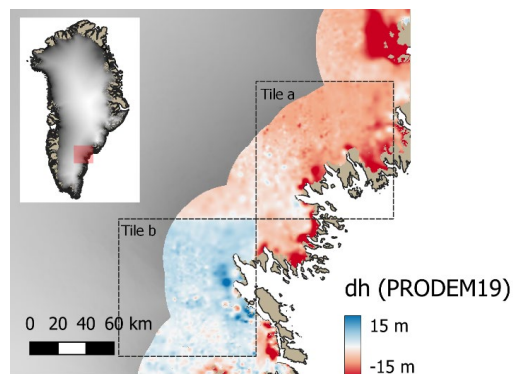
**Figure 10: Elevation anomalies (here for PRODEM19) relative to ArcticDEM display a checkerboard pattern due to the way ArcticDEM was constructed. Two ArcticDEM tiles of 100x100km are indicated.**

Errors and artefacts in ArcticDEM will influence the interpolated elevation field, and remnants of the checkerboard pattern of

595 retrieved elevation anomalies may still to some extent be visible in the PRODEMs. Of greater concern, however, are localized abrupt changes in the elevation anomaly, since these will affect the interpolation over an extended area. For this reason, we removed IS2 observations flagged as outliers in the elevation anomaly field (section 5.2), despite our belief that most of the large elevation anomalies are caused by local errors in ArcticDEM. One case concerns an area north of Korridoren Glacier in East Greenland, where the altimetry observations in several very localized areas (1-2km; an example is shown in Fig. 11)

600 consistently measure much lower elevation values (~1450m) than present in ArcticDEM (>4000m). The area is located just west of a large mountainside protruding from the ice sheet, and we suspect that undetected low-lying clouds in the employed stereo-imagery for this area have caused issues for the algorithms behind ArcticDEM. Similar other areas exist in this neighbourhood. Incorporating the IS2 data for these areas would violate the assumption of spatial continuity of the variable being interpolated, which is a requirement for kriging to produce robust results. We note, however, that by filtering these data

605 out beforehand, we also remove the opportunity of using the PRODEMs to detect such large-discrepancy areas in ArcticDEM. A more promising way forward might be to use these data to correct ArcticDEM in these localized areas before interpolation.
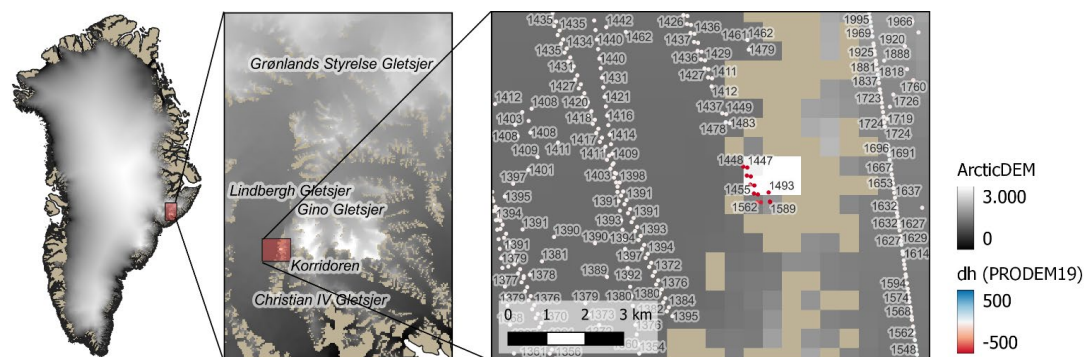
**Figure 11: An area close to Korridoren Glacier (location indicated in the overview maps) showing very high variability of the**
610 **observed elevation anomalies relative to ArcticDEM (grey-scale; shown for areas within the applied ice mask). Taupe areas are not covered by ice according to the applied ice mask. Altimetry observations are labelled based on their elevations and coloured based on the associated elevation anomalies. A localized area of very high (>500m) elevation anomalies exists, which we attribute to errors in ArcticDEM. Elevation anomaly data from summer 2019.**

The PRODEMs also exhibit artefacts caused by temporal differences in data acquisition. The altimetry data is collected during
615    a four-month period, during which the surface elevation may change due to e.g. snowfall and surface melt. As a result of this,
we observe a slightly striped pattern in the PRODEMs in some areas, seemingly aligned with the IS2 satellite tracks (Fig. 12a-
b). The difference in elevation across the stripes is less than half a meter, and within the uncertainty of the resulting elevation
field. Investigating the source of this pattern, we observe that it often occurs where two closely spaced IS2 satellite tracks are
obtained at the beginning and end of the summer season, respectively. Indeed, the observations along the two tracks may differ
620    in average elevation by up to a meter. The interpolated surface in the area between the satellite tracks depends on which line
of IS2 observations is closest. This can also be seen from the changes in the weighted mean acquisition time of the input data
used in the interpolation across the area: A striped pattern similar to that in the elevation anomalies is evident from the day-
of-year field (Fig 12c). Not all locations with large variability in average time of data acquisition are prone to form this stripy
pattern. The pattern is only visible in areas where the surface elevation has changed significantly during the summer period,
625    and where the surface characteristics are described by a short variogram length scale, so that only the closest data points are
given a high weight during interpolation.
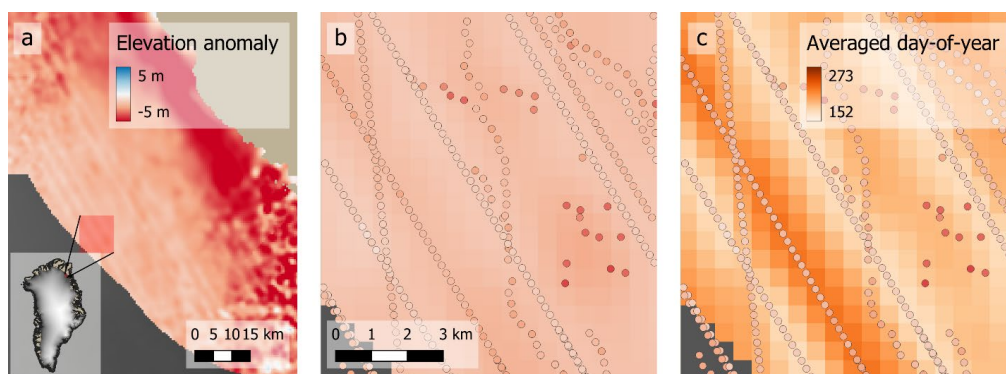
**Figure 12: A slightly striped pattern in elevation anomalies is caused by differences in time of data acquisition. a, b) 2019 elevation**
630    **anomalies in a small area of northeast Greenland (red box in the overview figure), with a zoom in (red box) to an even smaller area.**
**Dots indicate the altimetry data based on which the interpolation is based and coloured according to the measured elevation**
**difference (same colour scale as the interpolated field). c) Averaged day-of-year represented by the interpolated surface; going from**
**June 1$^{st}$ (day: 152) to September 30$^{th}$ (day: 273) in 2019.**

## 10 Data products and availability

635    The PRODEMs described in this manuscript can be accessed at https://doi.org/10.22008/FK2/52WWHG (Winstrup, 2023).
Presently, the product covers summers 2019 through 2022. The product is expected to be updated annually over the coming
years.

Each annual 500m resolution PRODEM is provided as a georeferenced (EPSG:3413) raster in GeoTIFF-format (.tif)
640    containing the following four data layers:

- *DEM:* PRODEMyy (in m)
- *variance:* Elevation uncertainty (field variance, in m)
- *dh:* Elevation anomalies (m) relative to the ArcticDEM v3 500m mosaic
- *time stamp:* Time-stamp associated with the interpolation (in units of day-of-year).

## 11 Conclusion

We have constructed an annual series of 500m resolution summer DEMs (PRODEMyy) for the marginal zone of the Greenland ice sheet. The DEMs are created by fusing satellite altimetry data from CryoSat-2 and ICESat-2, and hence the PRODEM series starts in 2019, the first summer after ICESat-2 became operational. The present PRODEM series consists of four DEMs, with the most current being from last summer (summer 2022), and we aim to repeat the procedure for the coming years to continually obtain annual changes in surface elevation across this rapidly changing region of the Greenland ice sheet.

The PRODEMs are interpolated using regionally varying kriging on elevation anomalies relative to the ArcticDEM mosaic, with spatially-varying uncertainties of the individual data points modelled based on a cross-over analysis of satellite tracks. This approach is able to account for the observed large regional differences in covariance structure of the anomaly field across the area. The PRODEMs are validated using leave-one-track-out cross-validation, and we find the obtained elevation fields to be well determined within their associated spatially varying uncertainties.

For most of the marginal zone, we observe a lowering of the ice sheet surface compared to ArcticDEM, albeit with large spatial differences: Almost all of West Greenland has experienced a lowering of the ice sheet surface, whereas extensive areas of increased elevations exist in East Greenland. Individual outlet glaciers may behave differently and may also change behaviour over time, illustrating their dynamical nature. We emphasize that since ArcticDEM is built from data from a regionally varying time window, the elevation differences between the PRODEMs and ArcticDEM cannot be directly converted to elevation change estimates. Indeed, some features in the elevation anomaly merely reflect artefacts related to the construction of ArcticDEM in tiles: We observe a checkerboard pattern in the derived elevation anomalies, with each tile having distinctly different mean anomaly fields.

The surface of the Greenland ice sheet has been experiencing a general lowering due to climate change, and on this trend is superimposed a complex and annually shifting pattern of changes due to glacier dynamics and mass balance processes. Directly accounting for the evolving ice topography across flux gates by applying the high-time-resolution PRODEM elevations will improve our estimates for the annual solid ice discharge from the ice sheet and allow us to much better capture its interannual variability caused by the year-to-year differences in snowfall and mass loss. By capturing the patterns of change in the marginal ice topography on an annual basis, the PRODEMs will also give valuable insights on the inter-annual variability of ice sheet dynamic processes and contribute to validation of ice sheet models.

**Author contributions.** MW developed the method, generated the DEMs, interpreted the results and wrote the manuscript with contributions from all co-authors. LSS initially conceived of the study and contributed with regular discussions and project guidance, the latter in collaboration with RSF. HR and SBS extracted datafiles with the IS2 and CS2 data and assisted with manuscript preparation. SHL, KDM provided valuable insights and significant revisions to the manuscript. All authors contributed to improving the final manuscript.

**Competing interests.** Ken Mankoff is a Chief Editor at ESSD. The authors declare that they otherwise have no conflict of interest.

**Acknowledgements.** ArcticDEM is provided by the Polar Geospatial Center under NSF-OPP awards 1043681, 1559691, and 1542736.

**Financial support.** This research has been supported by the Programme for Monitoring of the Greenland Ice Sheet (PROMICE).

## References

690 Ahlstrøm, A. P. , and the PROMICE project team: Geological Survey of Denmark and Greenland Bulletin 15, 2008, 61-64, Geological Survey of Denmark and Greenland Bulletin, 15, 61–64, 2008.

Bales, R. C., McConnell, J. R., Mosley-Thompson, E., and Csatho, B.: Accumulation over the Greenland ice sheet from historical and recent records, Journal of Geophysical Research Atmospheres, 106, 33813–33825, https://doi.org/10.1029/2001JD900153, 2001.

695 Bamber, J. L., Layberry, R. L., and Gogineni, S. P.: A new ice thickness and bed data set for the Greenland ice sheet: 1. Measurement, data reduction, and errors, Journal of Geophysical Research Atmospheres, 106, 33773–33780, https://doi.org/10.1029/2001JD900054, 2001.

Bjørk, A. A., Kruse, L. M., and Michaelsen, P. B.: Brief communication: Getting Greenland's glaciers right - A new data set of all official Greenlandic glacier names, Cryosphere, 9, 2215–2218, https://doi.org/10.5194/tc-9-2215-2015, 2015.

700 Van Den Broeke, M., Bamber, J., Ettema, J., Rignot, E., Schrama, E., Van Berg, W. J. De, Van Meijgaard, E., Velicogna, I., and Wouters, B.: Partitioning recent Greenland mass loss, Science (1979), 326, 984–986, https://doi.org/10.1126/science.1178176, 2009.

Brunt, K. M., Neumann, T. A., and Smith, B. E.: Assessment of ICESat-2 Ice Sheet Surface Heights, Based on Comparisons Over the Interior of the Antarctic Ice Sheet, Geophys Res Lett, 46, 13072–13078, https://doi.org/10.1029/2019GL084886,
705 2019.

Cressie, N. A. C.: Spatial Prediction and Kriging, in: Statistics for Spatial Data, 105–209, https://doi.org/https://doi.org/10.1002/9781119115151.ch3, 1993.

ESA: CryoSat-2 Product Handbook Baseline D 1.1, https://earth.esa.int/web/guest/document-library/browse-document-library/-/article/cryosat-baseline-d-ice-product-handbook, 2019.

710 ESA: CryoSat-2 Product Handbook, Baseline E 1.0, Draft B, 1–71 pp., 2021.

Fan, Y., Ke, C. Q., and Shen, X.: A new Greenland digital elevation model derived from ICESat-2 during 2018-2019, Earth Syst Sci Data, 14, 781–794, https://doi.org/10.5194/essd-14-781-2022, 2022.

Fausto, R. S. and the PROMICE team: The Greenland ice sheet - snowline elevations at the end of the melt seasons from 2000 to 2017, Geological Survey of Denmark and Greenland Bulletin, 41, 71–74, https://doi.org/10.34194/geusb.v41.4346, 2018.

715 Groh, A., Horwath, M., Horvath, A., Meister, R., Sørensen, L. S., Barletta, V. R., Forsberg, R., Wouters, B., Ditmar, P., Ran, J., Klees, R., Su, X., Shang, K., Guo, J., Shum, C. K., Schrama, E., and Shepherd, A.: Evaluating GRACE mass change time series for the antarctic and Greenland ice sheet-methods and results, Geosciences (Switzerland), 9, https://doi.org/10.3390/geosciences9100415, 2019.

Hengl, T. H.: A Practical Guide to Geostatistical Mapping, 2009.

720 Hurkmans, R. T. W. L., Bamber, J. L., and Griggs, J. A.: Brief communication: "Importance of slope-induced error correction in volume change estimates from radar altimetry," Cryosphere, 6, 447–451, https://doi.org/10.5194/tc-6-447-2012, 2012.

Karlsson, N. B., Solgaard, A. M., Mankoff, K. D., Gillet-Chaulet, F., MacGregor, J. A., Box, J. E., Citterio, M., Colgan, W. T., Larsen, S. H., Kjeldsen, K. K., Korsgaard, N. J., Benn, D. I., Hewitt, I. J., and Fausto, R. S.: A first constraint on basal melt-water production of the Greenland ice sheet, Nat Commun, 12, https://doi.org/10.1038/s41467-021-23739-z, 2021.

725 King, M. D., Howat, I. M., Candela, S. G., Noh, M. J., Jeong, S., Noël, B. P. Y., van den Broeke, M. R., Wouters, B., and Negrete, A.: Dynamic ice loss from the Greenland Ice Sheet driven by sustained glacier retreat, Commun Earth Environ, 1, https://doi.org/10.1038/s43247-020-0001-2, 2020.

Levinsen, J. F., Simonsen, S. B., Sorensen, L. S., and Forsberg, R.: The Impact of DEM Resolution on Relocating Radar Altimetry Data over Ice Sheets, IEEE J Sel Top Appl Earth Obs Remote Sens, 9, 3158–3163, https://doi.org/10.1109/JSTARS.2016.2587684, 2016.

MacGregor, J. A., Fahnestock, M. A., Catania, G. A., Paden, J. D., Prasad Gogineni, S., Young, S. K., Rybarski, S. C., Mabrey, A. N., Wagman, B. M., and Morlighem, M.: Radiostratigraphy and age structure of the Greenland Ice Sheet, J Geophys Res Earth Surf, 120, 212–241, https://doi.org/10.1002/2014JF003215, 2015.

Magruder, L. A., Brunt, K. M., and Alonzo, M.: Early icesat-2 on-orbit geolocation validation using ground-based corner cube retro-reflectors, Remote Sens (Basel), 12, 1–21, https://doi.org/10.3390/rs12213653, 2020.

Mankoff, K. D., Colgan, W., Solgaard, A., Karlsson, N. B., Ahlstrøm, A. P., Van As, D., Box, J. E., Abbas Khan, S., Kjeldsen, K. K., Mouginot, J., and Fausto, R. S.: Greenland Ice Sheet solid ice discharge from 1986 through 2017, Earth Syst Sci Data, 11, 769–786, https://doi.org/10.5194/essd-11-769-2019, 2019.

Mankoff, K. D., Fettweis, X., Langen, P. L., Stendel, M., Kjeldsen, K. K., Karlsson, N. B., Noël, B., Van Den Broeke, M. R., Solgaard, A., Colgan, W., Box, J. E., Simonsen, S. B., King, M. D., Ahlstrøm, A. P., Andersen, S. B., and Fausto, R. S.: Greenland ice sheet mass balance from 1840 through next week, Earth Syst Sci Data, 13, 5001–5025, https://doi.org/10.5194/essd-13-5001-2021, 2021.

Markus, T., Neumann, T., Martino, A., Abdalati, W., Brunt, K., Csatho, B., Farrell, S., Fricker, H., Gardner, A., Harding, D., Jasinski, M., Kwok, R., Magruder, L., Lubin, D., Luthcke, S., Morison, J., Nelson, R., Neuenschwander, A., Palm, S., Popescu, S., Shum, C. K., Schutz, B. E., Smith, B., Yang, Y., and Zwally, J.: The Ice, Cloud, and land Elevation Satellite-2 (ICESat-2): Science requirements, concept, and implementation, Remote Sens Environ, 190, 260–273, https://doi.org/10.1016/j.rse.2016.12.029, 2017.

McMillan, M., Leeson, A., Shepherd, A., Briggs, K., Armitage, T. W. K., Hogg, A., Kuipers Munneke, P., van den Broeke, M., Noël, B., van de Berg, W. J., Ligtenberg, S., Horwath, M., Groh, A., Muir, A., and Gilbert, L.: A high-resolution record of Greenland mass balance, Geophys Res Lett, 43, 7002–7010, https://doi.org/10.1002/2016GL069666, 2016.

Meloni, M., Bouffard, J., Parrinello, T., Dawson, G., Garnier, F., Helm, V., Di Bella, A., Hendricks, S., Ricker, R., Webb, E., Wright, B., Nielsen, K., Lee, S., Passaro, M., Scagliola, M., Bjerregaard Simonsen, S., Sandberg Sørensen, L., Brockley, D., Baker, S., Fleury, S., Bamber, J., Maestri, L., Skourup, H., Forsberg, R., and Mizzi, L.: CryoSat Ice Baseline-D validation and evolutions, Cryosphere, 14, 1889–1907, https://doi.org/10.5194/tc-14-1889-2020, 2020.

Moon, T., Ahlstrøm, A., Goelzer, H., Lipscomb, W., and Nowicki, S.: Rising Oceans Guaranteed: Arctic Land Ice Loss and Sea Level Rise, https://doi.org/10.1007/s40641-018-0107-0, 1 September 2018.

Morlighem, M., Williams, C. N., Rignot, E., An, L., Arndt, J. E., Bamber, J. L., Catania, G., Chauché, N., Dowdeswell, J. A., Dorschel, B., Fenty, I., Hogan, K., Howat, I., Hubbard, A., Jakobsson, M., Jordan, T. M., Kjeldsen, K. K., Millan, R., Mayer, L., Mouginot, J., Noël, B. P. Y., O'Cofaigh, C., Palmer, S., Rysgaard, S., Seroussi, H., Siegert, M. J., Slabon, P., Straneo, F., van den Broeke, M. R., Weinrebe, W., Wood, M., and Zinglersen, K. B.: BedMachine v3: Complete Bed Topography and Ocean Bathymetry Mapping of Greenland From Multibeam Echo Sounding Combined With Mass Conservation, Geophys Res Lett, 44, 11,051-11,061, https://doi.org/10.1002/2017GL074954, 2017.

Morlighem, M., Williams, C., Rignot, E., An, L., Arndt, J. E., Bamber, J., Catania, G., Chauché, N., Dowdeswell, J. A. , Dorschel, B., Fenty, I., Hogan, K., Howat, I., Hubbard, A., Jakobsson, M., Jordan, T. M., Kjeldsen, K. K., Millan, R., Mayer, L., Mouginot, J., Noël, B. , O'Cofaigh, C., Palmer, S. J., Rysgaard, S., Seroussi, H., Siegert, M. J., Slabon, P., Straneo, F., van den  Broeke, M. R., Weinrebe, W., Wood, M., and Zinglersen, K.: IceBridge BedMachine Greenland, Version  5, allsubsets used, https://doi.org/https://doi.org/10.5067/GMEVBWFLWA7X, 2022.

Mouginot, erémie, Rignot, E., Bjørk, A. A., van den Broeke, M., Millan, R., Morlighem, M., Nö el, B., Scheuchl, B., and Wood, M.: Forty-six years of Greenland Ice Sheet mass balance from 1972 to 2018, 116, 9239–9244, https://doi.org/10.7280/D1MM37, 2019.

Müller, S., Schüler, L., Zech, A., and Heße, F.: GSTools v1.3: A toolbox for geostatistical modelling in Python, Geosci Model Dev, 15, 3161–3182, https://doi.org/10.5194/gmd-15-3161-2022, 2022.

Nagler, T., Rott, H., Hetzenecker, M., Wuite, J., and Potin, P.: The Sentinel-1 mission: New opportunities for ice sheet observations, Remote Sens (Basel), 7, 9371–9389, https://doi.org/10.3390/rs70709371, 2015.

775 Noh, M. J. and Howat, I. M.: Automated stereo-photogrammetric DEM generation at high latitudes: Surface Extraction with TIN-based Search-space Minimization (SETSM) validation and demonstration over glaciated regions, GIsci Remote Sens, 52, 198–217, https://doi.org/10.1080/15481603.2015.1008621, 2015.

NSIDC: User Notice: Geolocation error in ATLAS/ICESat-2 data sets at NSIDC DAAC, https://nsidc.org/data/user-resources/data-announcements/user-notice-geolocation-error-atlasicesat-2-data-sets-nsidc-daac, 10 March 2023.

780 Otosaka, I. N., Shepherd, A., Ivins, E. R., Schlegel, N.-J., Amory, C., van den Broeke, M. R., Horwath, M., Joughin, I., King, M. D., Krinner, G., Nowicki, S., Payne, A. J., Rignot, E., Scambos, T., Simon, K. M., Smith, B. E., Sørensen, L. S., Velicogna, I., Whitehouse, P. L., A, G., Agosta, C., Ahlstrøm, A. P., Blazquez, A., Colgan, W., Engdahl, M. E., Fettweis, X., Forsberg, R., Gallée, H., Gardner, A., Gilbert, L., Gourmelen, N., Groh, A., Gunter, B. C., Harig, C., Helm, V., Khan, S. A., Kittel, C., Konrad, H., Langen, P. L., Lecavalier, B. S., Liang, C.-C., Loomis, B. D., McMillan, M., Melini, D., Mernild, S. H., Mottram, 785 R., Mouginot, J., Nilsson, J., Noël, B., Pattle, M. E., Peltier, W. R., Pie, N., Roca, M., Sasgen, I., Save, H. V., Seo, K.-W., Scheuchl, B., Schrama, E. J. O., Schröder, L., Simonsen, S. B., Slater, T., Spada, G., Sutterley, T. C., Vishwakarma, B. D., van Wessem, J. M., Wiese, D., van der Wal, W., and Wouters, B.: Mass balance of the Greenland and Antarctic ice sheets from 1992 to 2020, Earth Syst Sci Data, 15, 1597–1616, https://doi.org/10.5194/essd-15-1597-2023, 2023.

Paciorek, C.: Technical Vignette 3: Kriging, interpolation, and uncertainty, 1–4 pp., 2008.

790 Parrinello, T., Shepherd, A., Bouffard, J., Badessi, S., Casal, T., Davidson, M., Fornari, M., Maestroni, E., and Scagliola, M.: CryoSat: ESA's ice mission – Eight years in space, Advances in Space Research, 62, 1178–1190, https://doi.org/10.1016/j.asr.2018.04.014, 2018.

PGC: PGC's DEM Products guide - ArcticDEM, REMA, and EarthDEM, https://www.pgc.umn.edu/guides/stereo-derived-elevation-models/pgcs-dem-products-arcticdem-rema-and-earthdem/.

795 Porter, C., Morin, P., Howat, I., Noh, M.-J., Bates, B., Peterman, K., Keesey, S., Schlenk, M., Gardiner, J., Tomko, K., Willis, M., Kelleher, C., Cloutier, M., Husby, E., Foga, S., Nakamura, H., Platson, M., Wethington Jr., M., Williamson, C., Bauer, G., Enos, J., Arnold, G., Kramer, W., Becker, P., Doshi, A., D'Souza, C., Cummens, P., Laurier, F., Bojesen, M., and Foundation, N. S.: ArcticDEM, Version 3, https://doi.org/doi/10.7910/DVN/OHHUKH, 2018.

Schröder, L., Horwath, M., Dietrich, R., Helm, V., Van Den Broeke, M. R., and Ligtenberg, S. R. M.: Four decades of Antarctic 800 surface elevation changes from multi-mission satellite altimetry, Cryosphere, 13, 427–449, https://doi.org/10.5194/tc-13-427-2019, 2019.

Shepherd, A., Ivins, E., Rignot, E., Smith, B., van den Broeke, M., Velicogna, I., Whitehouse, P., Briggs, K., Joughin, I., Krinner, G., Nowicki, S., Payne, T., Scambos, T., Schlegel, N., A, G., Agosta, C., Ahlstrøm, A., Babonis, G., Barletta, V. R., Bjørk, A. A., Blazquez, A., Bonin, J., Colgan, W., Csatho, B., Cullather, R., Engdahl, M. E., Felikson, D., Fettweis, X., 805 Forsberg, R., Hogg, A. E., Gallee, H., Gardner, A., Gilbert, L., Gourmelen, N., Groh, A., Gunter, B., Hanna, E., Harig, C., Helm, V., Horvath, A., Horwath, M., Khan, S., Kjeldsen, K. K., Konrad, H., Langen, P. L., Lecavalier, B., Loomis, B., Luthcke, S., McMillan, M., Melini, D., Mernild, S., Mohajerani, Y., Moore, P., Mottram, R., Mouginot, J., Moyano, G., Muir, A., Nagler, T., Nield, G., Nilsson, J., Noël, B., Otosaka, I., Pattle, M. E., Peltier, W. R., Pie, N., Rietbroek, R., Rott, H., Sandberg Sørensen, L., Sasgen, I., Save, H., Scheuchl, B., Schrama, E., Schröder, L., Seo, K. W., Simonsen, S. B., Slater, T., 810 Spada, G., Sutterley, T., Talpe, M., Tarasov, L., van de Berg, W. J., van der Wal, W., van Wessem, M., Vishwakarma, B. D., Wiese, D., Wilton, D., Wagner, T., Wouters, B., and Wuite, J.: Mass balance of the Greenland Ice Sheet from 1992 to 2018, Nature, 579, 233–239, https://doi.org/10.1038/s41586-019-1855-2, 2020.

Simonsen, S. B., Barletta, V. R., Colgan, W. T., and Sørensen, L. S.: Greenland Ice Sheet Mass Balance (1992–2020) From Calibrated Radar Altimetry, https://doi.org/10.1029/2020GL091216, 16 February 2021.

815 Smith, B., Fricker, H. A., Holschuh, N., Gardner, A. S., Adusumilli, S., Brunt, K. M., Csatho, B., Harbeck, K., Huth, A., Neumann, T., Nilsson, J., and Siegfried, M. R.: Land ice height-retrieval algorithm for NASA's ICESat-2 photon-counting laser altimeter, Remote Sens Environ, 233, 111352, https://doi.org/10.1016/j.rse.2019.111352, 2019.

Smith, B., Adusumilli, S., Csathó, M., Felikson, D., Fricker, H. A., Gardner, A., Holschuh, N., Lee, J., Nilsson, J., Paolo, F. S., Siegfried, M. R., Sutterley, T., and the ICESat-2 Science Team: ATLAS/ICESat-2 L3A Land Ice Height, Version 5 [Data

820 Set]., 2021.

Solgaard, A., Kusk, A., Boncori, J. P. M., Dall, J., Mankoff, K. D., Ahlstrøm, A. P., Andersen, S. B., Citterio, M., Karlsson, N. B., Kjeldsen, K. K., Korsgaard, N. J., Larsen, S. H., and Fausto, R. S.: Greenland ice velocity maps from the PROMICE project, Earth Syst Sci Data, 13, 3491–3512, https://doi.org/10.5194/essd-13-3491-2021, 2021.

Sørensen, L. S., Simonsen, S. B., Nielsen, K., Lucas-Picher, P., Spada, G., Adalgeirsdottir, G., Forsberg, R., and Hvidberg, C.

825 S.: Mass balance of the Greenland ice sheet (2003-2008) from ICESat data - The impact of interpolation, sampling and firn density, Cryosphere, 5, 173–186, https://doi.org/10.5194/tc-5-173-2011, 2011.

Sørensen, L. S., Simonsen, S. B., Forsberg, R., Khvorostovsky, K., Meister, R., and Engdahl, M. E.: 25 years of elevation changes of the Greenland Ice Sheet from ERS, Envisat, and CryoSat-2 radar altimetry, Earth Planet Sci Lett, 495, 234–241, https://doi.org/10.1016/j.epsl.2018.05.015, 2018.

830 Stein, M. L.: Interpolation of Spatial Data: Some Theory for Kriging, Springer Series in Statistics, Springer Science+Business Media, New York, https://doi.org/10.1007/978-1-4612-1494-6, 1999.

Velicogna, I., Mohajerani, Y., Geruo, A., Landerer, F., Mouginot, J., Noel, B., Rignot, E., Sutterley, T., van den Broeke, M., van Wessem, M., and Wiese, D.: Continuity of Ice Sheet Mass Loss in Greenland and Antarctica From the GRACE and GRACE Follow-On Missions, Geophys Res Lett, 47, https://doi.org/10.1029/2020GL087291, 2020.

835 Wang, F., Bamber, J. L., and Cheng, X.: Accuracy and Performance of CryoSat-2 SARIn Mode Data Over Antarctica, IEEE Geoscience and Remote Sensing Letters, 12, 1516–1520, https://doi.org/10.1109/LGRS.2015.2411434, 2015.

WCRP Global Sea Level Budget Group: Global sea-level budget 1993-present, https://doi.org/10.5194/essd-10-1551-2018, 28 August 2018.

Wingham, D. J., Francis, C. R., Baker, S., Bouzinac, C., Brockley, D., Cullen, R., de Chateau-Thierry, P., Laxon, S. W.,

840 Mallow, U., Mavrocordatos, C., Phalippou, L., Ratier, G., Rey, L., Rostan, F., Viau, P., and Wallis, D. W.: CryoSat: A mission to determine the fluctuations in Earth's land and marine ice fields, Advances in Space Research, 37, 841–871, https://doi.org/10.1016/j.asr.2005.07.027, 2006.

Winstrup, M.: PRODEM: Annual summer DEMs of the marginal areas of the Greenland Ice Sheet V1.0 [Dataset], https://doi.org/10.22008/FK2/52WWHG, 2023.

845 Zwally, H. J., Giovinetto, M. B., Beckley, M. A., and Saba, J. L.: Antarctic and Greenland Drainage Systems, 2012.